LA-UR-24-24989
Accepted Manuscript

Large-scale Structure of the Heliospheric Current Sheets within the Heliosheath Inferred from Voyager 2 Observations

Choi, Dooyoung
Lee, Dae-Young
Choi, Kyung-Eun
Noh, Sung Jun
Kim, Kyung-Chan

To be published in: The Astrophysical Journal

DOI to publisher's version: 10.3847/1538-4357/ad6e82

Permalink to record:
https://permalink.lanl.gov/object/view?what=info:lanl-repo/lareport/LA-UR-24-24989

The Astrophysical Journal, 974:152 (13pp), 2024 October 20 https://doi.org/10.3847/1538-4357/ad6e82

Large-scale Structure of the Heliospheric Current Sheets within the Heliosheath Inferred from Voyager 2 Observations

Dooyoung Choi[1], Dae-Young Lee[1], Kyung-Eun Choi[2], Sung Jun Noh[3], and Kyung-Chan Kim[1]
[1] Department of Astronomy and Space Science, Chungbuk National University, Chungbuk 28644, Republic of Korea
[2] Space Sciences Laboratory, University of California, Berkeley, CA, USA
[3] ISR-1: Space Science and Applications, Los Alamos National Laboratory, NM, USA
Received 2024 May 20; revised 2024 July 21; accepted 2024 August 11; published 2024 October 10

Abstract

In this paper, we conducted an analysis of the heliospheric current sheets (HCSs) in the heliosheath (HS), utilizing observations by Voyager 2 between 2008 and 2018. Employing rigorous criteria, we identified a total of 34 HCSs that indicate significant changes in magnetic polarity. These occurrences were more prevalent during solar maximum periods when the HCS expanded to higher latitudes, coinciding with the spacecraft positioned at an average latitude of $-31°$ from the solar equator. We determined certain features of the large-scale structures of the identified HCSs. Most importantly, employing two distinct methods indicates that the thickness of the HCSs within the HS ranges from $\sim$0.003 to $\sim$0.4 au with an average thickness of $\sim$0.03 to $\sim$0.1 au, depending on methods of event selection and fitting techniques. This thickness surpasses that known near 1 au or other heliospheric distances. It is also notably thicker than the typical proton inertial length, implying unfavorable conditions for magnetic reconnection. Additionally, our analysis reveals a frequent tilt of HCS planes relative to the solar equatorial plane by a varying angle up to several tens of degrees, likely implying a common occurrence of a warped structure of the HCS within the HS. Longitudinally, the HCS planes closely align with the Parker spiral field direction expected in the HS. Finally, for a large fraction of the identified HCS events, the HCS planes are likely characterized by a rotational discontinuity. These findings are valid within the limits of the 1 hr resolution data used in this study.

Unified Astronomy Thesaurus concepts: Heliosphere (711); Heliosheath (710)

1. Introduction

The heliospheric current sheet (HCS) is a spatial boundary that marks the reversal of the direction of the magnetic field originating from the Sun. Following the discovery of magnetic sectors in space by J. M. Wilcox & N. F. Ness (1965), observed through IMP 1, H. Alfvén (1977) proposed that these magnetic sectors, characterized by inward and outward magnetic fields, are separated by a current sheet surrounding the Sun. He suggested that these current sheets, identified as the discontinuous physical counterparts of sector boundaries, resemble a "ballerina's skirt." Until then, considerations of the HCS were confined to the near solar equatorial plane due to spacecraft orbit constraints. However, Pioneer 11 observations (E. J. Smith et al. 1978) provided crucial evidence for the inclined HCS at locations near up to 16° N of heliographic latitude. Indeed, it has been known that during solar maximum, the HCS expands to higher latitudes, while during solar minimum, it resides at lower latitudes (J. R. Jokipii & Thomas 1981; J. T. Hoeksema 1995). Consequently, the position of spacecraft becomes pivotal in HCS observations, making it possible miss during solar minimum for spacecraft with large heliographic latitudes. Furthermore, the HCS is known for its frequent observation of warped structures and multicrossing (K. W. Behannon et al. 1981; R. P. Lepping et al. 1996; C. Foullon et al. 2009; K. Liou & C.-C. Wu 2021).

When observing HCS crossings, it is known that there is a decrease in the intensity of the magnetic field and solar wind speed, while proton density and plasma beta exhibit an increase (G. Borrini et al. 1981; J. T. Gosling et al. 1981; D. Winterhalter et al. 1994; E. J. Smith 2001; S. T. Suess et al. 2009; K. D. C. Simunac et al. 2012; V. V. Zharkova & O. V. Khabarova 2012; O. Khabarova et al. 2015; K. Liou & C.-C. Wu 2021). The decrease in the magnetic field intensity and enhanced plasma flow have been the focus of numerous studies, expected to be associated with magnetic reconnection. Cases revealing evidence for magnetic reconnection at the HCSs close to the Sun have been reported through observations by the Parker Solar Probe (PSP; T. D. Phan et al. 2020, 2021).

The thickness of HCSs identified at varying distances, ranging from close proximity to the Sun to several au, has been observed to span a wide range from $\sim 10^3$ km to $\sim 10^6$ km (B. Bavassano et al. 1976; E. J. Smith et al. 1978; L. Klein & Burlaga 1980; K. W. Behannon et al. 1981; U. Villante & R. Bruno 1982; D. Winterhalter et al. 1994; R. P. Lepping et al. 1996; J. J. Blanco et al. 2008; T. D. Phan et al. 2020, 2021; K. Liou & C.-C. Wu 2021; D. Arrazola et al. 2022). Previous studies indicate a rather wide latitudinal distribution of normal vectors to the HCSs identified at 1 au (S. Shodhan et al. 1994; R. P. Lepping et al. 1996; J. J. Blanco et al. 2008; K. Liou & C.-C. Wu 2021; D. Arrazola et al. 2022). Additionally, the longitudinal orientation of the normal vector to the HCS planes has been found to be mostly perpendicular to the Parker spiral field (B. T. Thomas & E. J. Smith 1981; R. P. Lepping et al. 1996; J. J. Blanco et al. 2008).

The HCS we refer to here is a large-scale structure emanating from the Sun, extending into outer space and reaching the edge of the heliosphere. A key question arises concerning whether the well-known characteristics of the HCS at distances closer to the Sun persist in the heliosheath (HS)

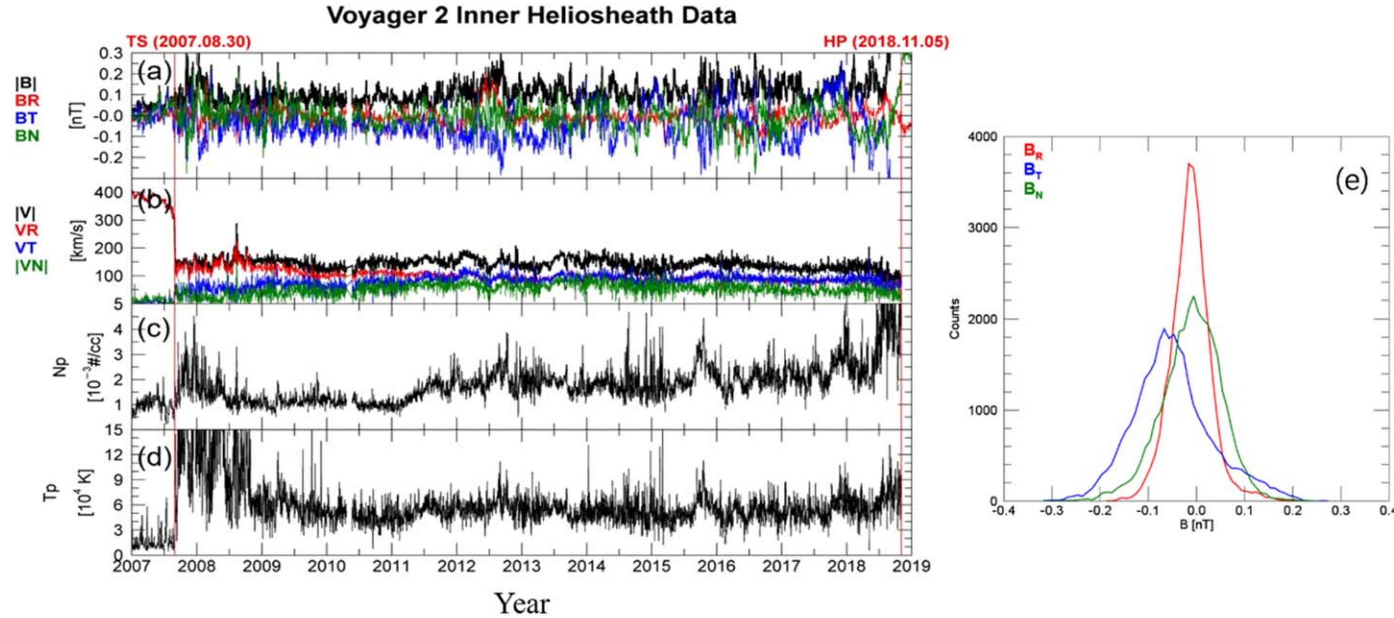

Figure 1. Observations of the magnetic field and plasma by Voyager 2 from 2007 to 2018. (a) Magnetic field intensity (black), and components B_R (red), B_T (blue), and B_N (green) in RTN coordinates. (b) Solar wind speed (black), and components V_R (red), V_T (blue), and $|V_N|$ (green) in RTN coordinates. (c) Solar wind proton density. (d) Proton temperature. The times of TS (termination shock) crossing and HP (heliopause) crossing are marked with red vertical lines. (e) Statistics of the magnetic field components during the HS interval. For the plots in panels (a)–(d), 1 day resolution data were used, and for the statistics in panel (e), 1 hr resolution data were used.

where the physical environment is different. The HS is the region between the termination shock (TS) and the heliopause (HP), initially observed in situ by Voyager 1 and 2. In this region, the solar wind speed decreases to subsonic levels, plasma density increases, and plasma temperature rises compared to the conditions observed before the TS. This area serves as the first encounter region for interstellar particles entering the heliosphere, creating a dense environment conducive to charge-exchange interactions with solar wind and pickup ion particles. Additionally, in contrast to physical characteristics in the vicinity of the Sun, studying this distant region enables inferences about the evolution of structures and phenomena originating from the Sun.

While there have been some studies examining the HCSs within the HS based on Voyager observations (L. F. Burlaga et al. 2017, 2018, 2021), L. F. Burlaga et al. (2016) notably categorized observable current sheets in the HS into four distinct categories: proton boundary layer, magnetic hump, magnetic hole, and sector boundary. However, there remains a dearth of comprehensive analyses regarding HCSs within the HS, including factors such as thickness and orientations, and the fundamental nature of HCS planes as discontinuities (to the best of the authors' knowledge).

In this paper, we identified HCS crossing events that were regarded as sector boundaries throughout the nearly entire duration of the HS observed by Voyager 2. We examined some of the basic physical characteristics at the crossing points and, most importantly, determined the thickness and orientation of the identified HCSs, and further examined whether the HCS planes are closer to a rotational discontinuity (RD) or a tangential discontinuity (TD). In Section 2, we first illustrate the method used to select the HCS events during the HS period, and describe some of the basic features of the identified HCS events. In Section 3, we present the estimated thickness and orientation of the HCS events and illustrate the extent to which the HCS planes are characterized by an RD. We then discuss key issues in Section 4 and conclude in Section 5.

2. Identification and Overview of HCS Events

In this study, we utilized magnetic field data (K. W. Behannon et al. 1977) and solar wind plasma data (H. S. Bridge et al. 1977) obtained from Voyager 2 observations. Due to the lack of continuous coverage with a high time resolution for the period spanning 2008–2018, our primary reliance is on 1 hr resolution data, complemented by supplementary 1 day resolution data. All the data used in this study is accessible through the public data archive NASA CDAWeb.[4]

Figures 1(a)–(d) show the daily averages of magnetic field and plasma data recorded by Voyager 2 spanning the years from 2007 to 2018. The two red vertical lines denote the crossing times of the TS on 2007 August 30 (E. C. Stone et al. 2008) and the HP on 2018 November 5 (E. C. Stone et al. 2019), respectively. As shown in Figure 1(a), the magnetic field intensity within the HS becomes larger compared to the upstream conditions before the TS. In addition, within the HS, the tangential component of the magnetic field, B_T, in RTN coordinates dominates, implying that the average direction of the magnetic field is close to the expected direction of the Parker spiral field. The solar wind speed drops substantially as Voyager 2 crosses the TS, as depicted in Figure 1(b). The density and temperature exhibit an increase in the HS compared to the period before the TS crossing (Figures 1(c) and (d), respectively). Due to the multiple crossings of the TS (L. F. Burlaga et al. 2008) and significant fluctuations near the TS and HP, in this study we used data from 2008 January 1 to 2018 June 30, while avoiding times close to the TS and HP. Figure 1(e) shows the statistical distributions of the magnetic field components within the HS. The statistics indicate the widest distribution in B_T largely skewed toward the negative regime and the most sharply peaked profile for B_R around zero. Table 1 summarizes some numbers indicating statistical

[4] https://cdaweb.gsfc.nasa.gov/pub/data/voyager

Table 1
Statistics of the Magnetic Field Components in the HS

Components	Mean	Standard Deviation	Absolute Mean[a]	Mean Absolute Deviation[b]
B_R	−0.008	0.042	0.032	0.031
B_T	−0.045	0.083	0.078	0.064
B_N	−0.006	0.063	0.049	0.049

Notes.
[a] Defined as $(1/N)\sum_{i=1}^{N}|x_i|$, where x refers to each of the magnetic field components.
[b] Defined as $(1/N)\sum_{i=1}^{N}|x_i - \langle x \rangle|$.

differences among the three components. The absolute mean values in Table 1 are largest for B_T, smaller for B_N by ∼30% compared to B_T, and smallest for B_R. It is also useful to mention that the fluctuations are most significant in B_T, smaller for B_N by ∼23% compared to B_T, and least for B_R, as inferred from the standard deviation and mean absolute deviation values in Table 1.

2.1. Identification Criteria

In this section, we elaborate on the method employed for identifying the HCSs. While various methods are available for this purpose, one particularly advantageous approach involves the use of suprathermal electrons. Prior studies have successfully employed this approach to identify the HCSs (N. U. Crooker et al. 2004; V. V. Zharkova & O. V. Khabarova 2012; A. Szabo et al. 2020; B. Lavraud et al. 2020; T. D. Phan et al. 2020, 2021). However, due to the absence of instruments on Voyager capable of measuring the pitch angle of suprathermal electrons, we solely relied on magnetic field data to identify HCS crossing events.

The digitization level and rms noise of the Voyager 2 magnetometers are 0.004 nT and 0.006 nT, respectively (K. W. Behannon et al. 1977), which suggest the capability to measure the magnetic field within the HS. However, given that the average magnetic field in the HS is around the 0.1 nT level, potentially influenced by the magnetic field generated by the spacecraft, uncertainties arise when using magnetic field data, as indicated in previous studies (L. F. Burlaga et al. 2002, 2014). Therefore, we applied stringent conditions, opting to include exclusively clear cases of HCS crossing events that qualify as sector boundaries, recognizing that the HCSs and sector boundaries may not always align (M. J. Owens et al. 2013; Y. C. -M. Liu et al. 2014; B. Lavraud et al. 2020; K. Liou & C.-C. Wu 2021).

At the outset, we obtained a list of candidate events of HCS crossing using 1 day resolution data. Specifically, we identified times when the sign of the magnetic field changed between a preceding 7 days period and a following 7 days period, but, to be practical, allowing for a brief deviation of polarity at one data point during each 7 days period. Considering that the tangential component of the magnetic field B_T is the dominant component in the HS, we first selected candidates based on the criterion that the difference in average B_T values between the preceding 7 days and the following 7 days periods exceeds 0.1 nT. We further required a substantial rotation of the magnetic field, contingent upon the condition that the variation of the azimuth angle of the magnetic field in the RTN coordinate system should be larger than 90° but less than 270°.

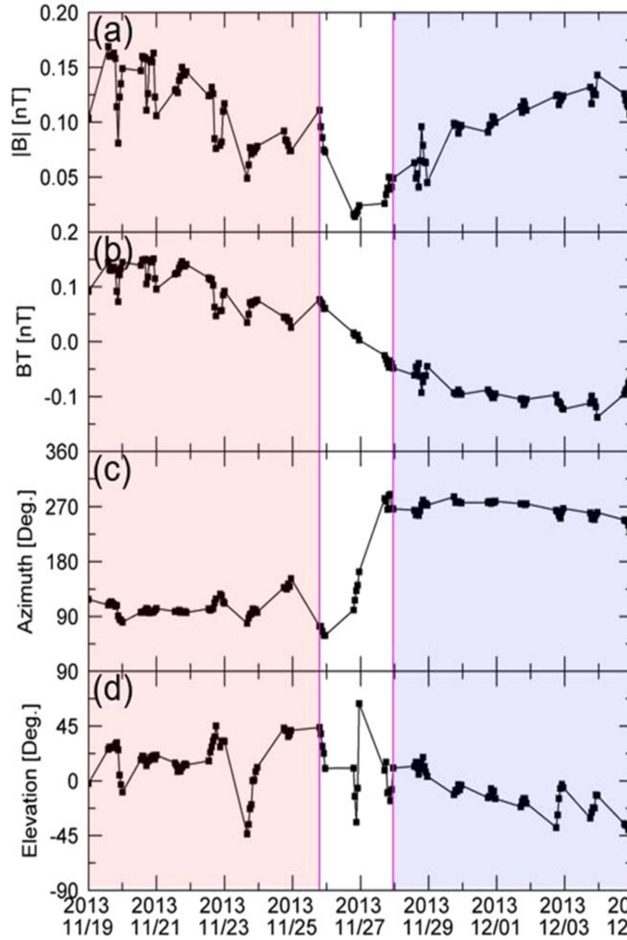

Figure 2. One of the identified HCS crossing events between 2013 November 25, and 2013 November 28. (a) Magnetic field intensity, (b) B_T component, (c) magnetic field azimuth angle, and (d) elevation angle. The magenta lines indicate the time interval when the azimuth angle undergoes a significant change, and the shaded intervals represent the preceding 7 days and following 7 days periods, respectively.

This additional requirement is useful to distinguish identified HCS events from other occurrences, such as the proton boundary layer (L. F. Burlaga et al. 2016). Following the selection of candidate events using the daily resolution data, we conducted a visual inspection of 1 hr resolution data to remove events exhibiting any anomalous behavior caused by irregular time intervals and more precisely determine the times of current sheet crossings. Through this process, a total of 24 HCS events were selected during the 11 yr that Voyager 2 traversed the HS.

Figure 2 illustrates an example out of the selected HCSs at 1 hr resolution. The magenta lines represent the approximate boundaries of the layer where the azimuth angle undergoes a notable change, a critical condition utilized in the event identification process. Figure 2(a) indicates that the intensity of the magnetic field during the crossing of the layer is lower compared to the vicinity of the crossing. Figure 2(b) illustrates the tangential component of the magnetic field B_T, showing a change in sign during the crossing. The azimuth angle, depicted in Figure 2(c), undergoes a 180° change during the identified HCS crossing interval. During this interval, the elevation angle remains close to zero, except for a sharp turning near the central time, as shown in Figure 2(d).

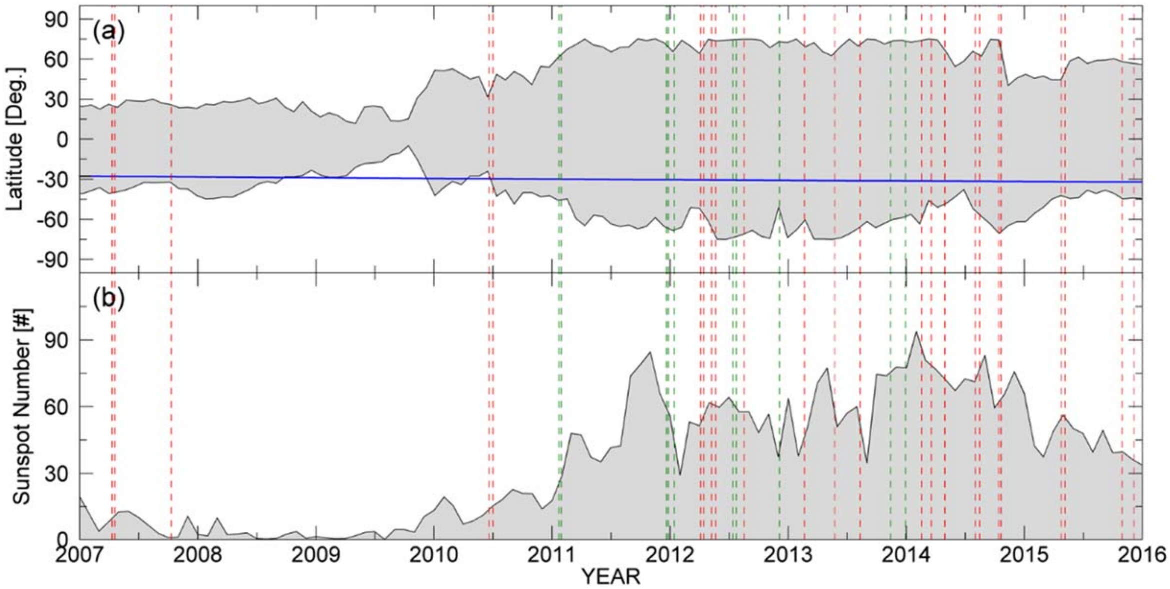

Figure 3. Distribution of the selected HCS events marked by the vertical lines (red for 24 events of the B_T-group and green for 10 events of the B_N-group). The event times are adjusted by considering the time shifts from the Voyager 2 locations to the Sun (see text for the details). In (a) the shaded region denotes the model latitude of the maximum extent of HCS (J. T. Hoeksema 1995, available at http://wso.stanford.edu/) and the horizontal blue line refers to the latitude of Voyager 2. In (b) monthly sunspot number is depicted for reference (http://www.swpc.noaa.gov).

Although the tangential component of the magnetic field is statistically the dominant component in the HS, to complement the analysis, we repeated the same process of event identification, now applying the selection criteria solely to the polarity change in the normal component of the magnetic field B_N. Consequently, we identified a total of 10 HCSs in the HS.

Finally, we identified no HCS events from the polarity changes of the radial component of the magnetic field (B_R) that met the identification criteria above.

As a result, we have identified two distinct groups of HCS events: one comprising 24 events derived from B_T polarity changes (referred to as the B_T-based group), and another comprising 10 events derived from B_N polarity changes (referred to as the B_N-based group). Among the 24 events of the B_T-based group, one-third are associated with simultaneous changes of B_N polarity to some extent. But the B_N polarity changes do not meet the selection criteria as HCS for all of these events except for one event in which the changes in both B_T and B_N polarities satisfy the criteria simultaneously. Among the 10 events of the B_N-based group, none of them are accompanied by B_T polarity changes that meet the selection criteria. Remarkably, for 8 out of the 10 events in the B_N-based group, the signs of B_T do not even change at all. Consequently, all but one of the identified HCS events in both groups are primarily characterized by directional changes in a single component of the magnetic field that meet our stringent conditions. Additionally, it is worth noting that the number of the identified HCS events is lower in the B_N-based group. We attribute this to the fact that the magnitude of B_N is overall smaller with less significant level of fluctuations compared to B_T, as shown in Figure 1 and Table 1. This results in a reduced chance of meeting our stringent selection criteria.

2.2. Overview of Identified Events

Figure 3 illustrates the times when the HCS events were selected (vertical red lines for the 24 events and vertical green lines for the 10 events). The illustration includes the HCS maximum extent model in latitude (J. T. Hoeksema 1995).[5] along with Voyager 2's latitude (the black curves enveloping the shaded area and the blue line in panel (a), respectively). The determination of the HCS maximum extent in latitude utilized the classic model (J. T. Hoeksema 1991). The identified HCS events are marked in Figure 3 as time-shifted from the spacecraft's locations in the HS to the Sun. For the time-shift, we used the average solar wind speed within the HS to propagate from the spacecraft back to the TS and used another average speed in the supersonic upstream solar wind for propagation from the TS to the Sun. The results in Figure 3 reveal that more HCS events were identified during solar maximum when the HCS extended to higher latitudes and no HCS crossing was identified in 2008 and 2009, corresponding to the solar minimum period. This observation aligns with Voyager 2's position at approximately $-31°$ in latitude in the heliographic inertial coordinate system, providing a reasonable explanation of the dependence of HCS crossing on the solar cycle.

Figure 4 shows the superposed epoch analysis of four major solar wind parameters during the identified HCS crossings, with 1 day resolution. The error bars represent 1 σ of all events. Significant standard deviations are observed for all four parameters. Only a weak trend is discernible across HCS crossings. Specifically, a decreasing magnetic field intensity (panel (a)) is identified, and a slight decrease in solar wind speed (panel (b)) may be discernible, although not too obvious. Moreover, there is a weak tendency for proton density to increase (panel (c)), whereas there is no clear trend in proton temperature (panel (d)). Additionally, we confirmed that the results of the superposed epoch analysis conducted with 1 hr resolution data exhibit a similar trend to the 1 day resolution data (not shown). While we acknowledge the identified trends are weak and subject to large standard deviations, they qualitatively align with findings

[5] Available at http://wso.stanford.edu/

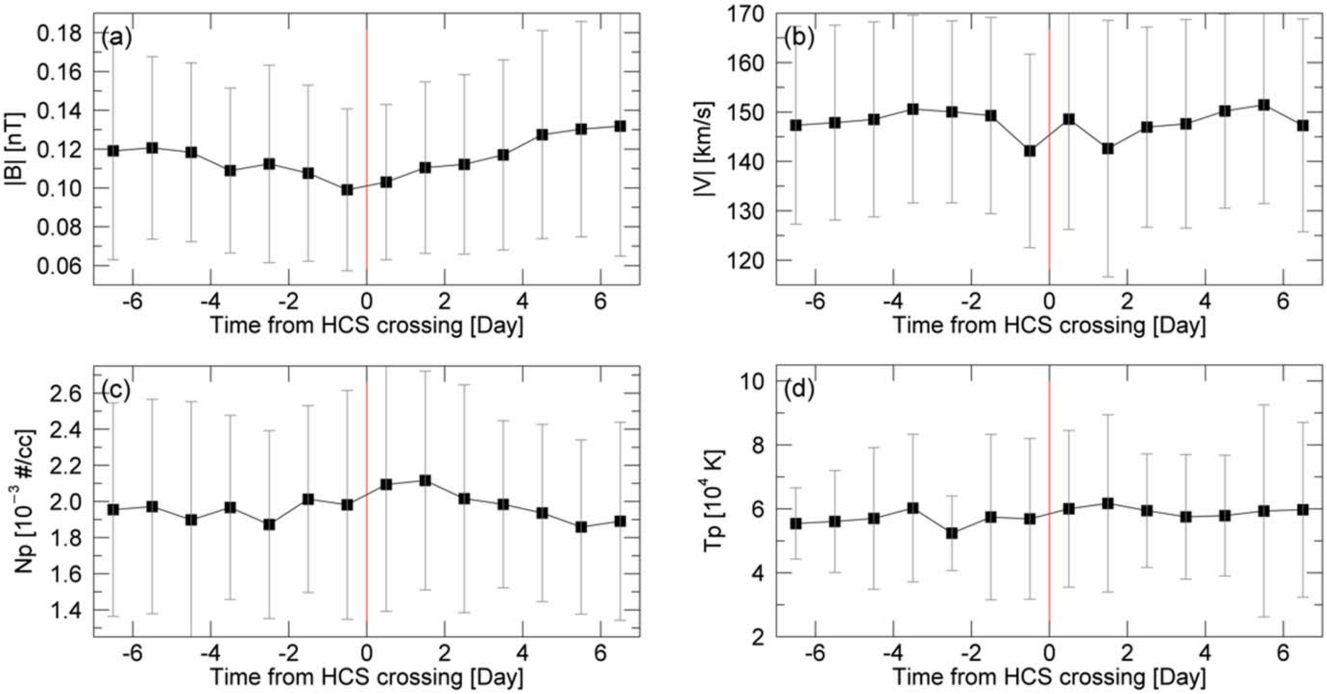

Figure 4. Results of the superposed epoch analysis with the total 34 HCS crossings for four major parameters, spanning from 7 days before to 7 days after the crossing. (a) Magnetic field intensity, (b) solar wind speed, (c) proton density, and (d) proton temperature.

from previous studies on HCSs near 1 au (S. T. Suess et al. 2009; K. Liou & C.-C.Wu 2021).

3. Thickness and Orientation of HCS Planes, and Nature of the Planes as a Discontinuity

We conducted an in-depth analysis of the identified HCS structure by utilizing 1 hr resolution magnetic field and plasma data. The analysis primarily focused on evaluating the thickness of the HCS and determining the latitude and longitude of the normal vectors to the HCS planes. Furthermore, we attempted to determine whether the HCS planes exhibits characteristics of an RD or a TD.

The orientation of the normal vector of the HCS is visually depicted in Figure 5. The latitude and longitude of the normal vector ($\hat{\boldsymbol{n}}$) were determined in the RTN coordinate system. Additionally, considering the position of Voyager 2 (average latitude of $-31°$ in the heliographic coordinate system), we calculated the inclination of the normal vector from the solar equatorial plane in the RTN coordinates. Notably, these key parameters (thickness and normal direction) were determined through two distinct methods, which will be described in the following section.

3.1. Analysis Methods

First, we employed a method referred to as the hyperbolic tangent rotation (HYTARO) algorithm (J. J. Blanco et al. 2003; D. Arrazola et al. 2022), which is based on a modified Harris current sheet model (E. J. Harris 1962). The Harris sheet is defined by the following set of equations:

$$B_x^{LS} = B_{0x} + B_A \tan h\left(\frac{y - y_0}{L}\right),$$
$$B_y^{LS} = B_{0y},$$
$$B_z^{LS} = B_{0z} \tag{1}$$

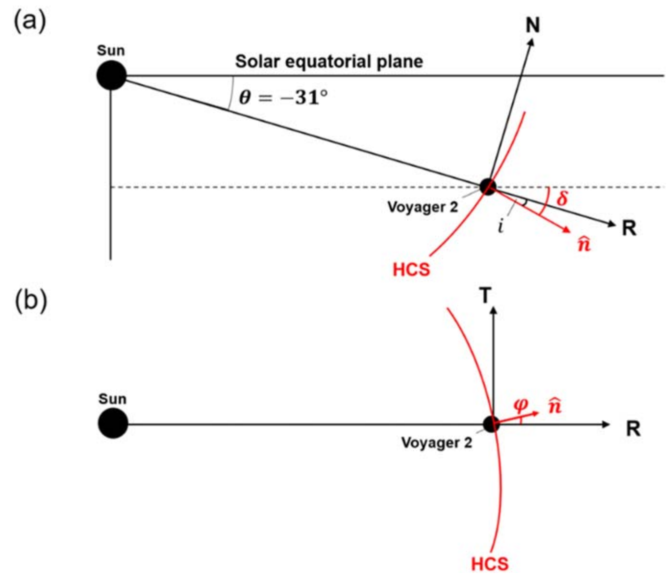

Figure 5. Illustration of the normal vector $\hat{\boldsymbol{n}}$ associated with an HCS plane. (a) Meridional plane view: The latitude of the normal vector, δ, is the angle between the solar equatorial plane and the normal vector, calculated as $\delta = i + \theta$. (b) Equatorial plane view: The longitude of the normal vector, φ, is the angle between the R direction and the normal vector.

where B_x^{LS}, B_y^{LS}, and B_z^{LS} represent the magnetic field components in the local coordinate system; B_{0x}, B_{0y}, and B_{0z} are constants; and B_A would represent the asymptotic value of the magnetic field at a large y distance, far away from the center of the current sheet, if the current sheet were described solely by the tan$h$ function. The parameter L represents half of the HCS thickness, and y_0 denotes the magnetic field inversion point. Considering the observed data in the RTN coordinates,

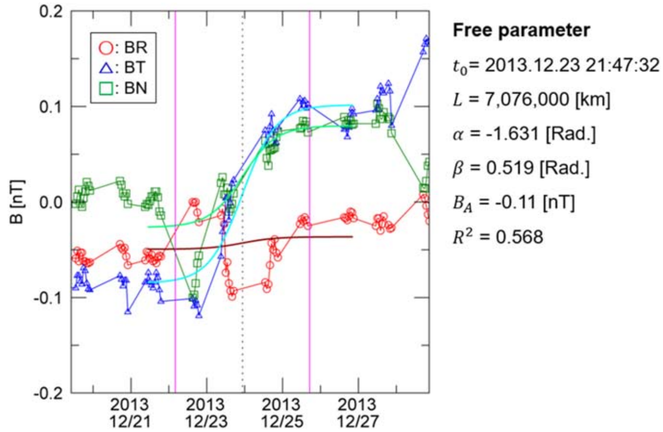

Figure 6. Observation of HCS crossing occurring between 2013 December 22, and 2013 December 25 (lines with symbols) to which the HYTARO fitting method (refer to the main text for details) was applied (solid curves).

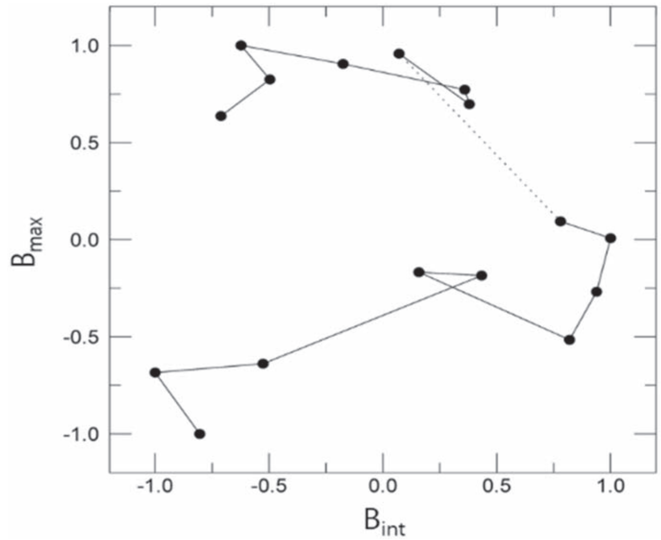

Figure 7. Magnetic field hodogram obtained from MVA applied to an HCS crossing interval between 2013 December 22, and 2013 December 25, which is the same interval as in Figure 6. The dotted line indicates the gap in the data. $\boldsymbol{B}_{\mathrm{int}}$ and $\boldsymbol{B}_{\max}$ values are normalized between −1 and 1.

the rotations of local coordinates by Euler angles α and β yields Equation (2):

$$\begin{aligned} B_R^{\mathrm{RTN}} &= \left[B_{0x} + B_A \tan h\left(\frac{(t-t_0)v}{L}\right) \right] \\ &\quad \cos\alpha - B_{0y}\sin\alpha, \\ B_T^{\mathrm{RTN}} &= \left\{ \left[B_{0x} + B_A \tan h\left(\frac{(t-t_0)v}{L}\right) \right] \right. \\ &\quad \left. \sin\alpha + B_{0y}\cos\alpha \right\} \cos\beta - B_{0z}\sin\beta, \\ B_N^{\mathrm{RTN}} &= \left\{ \left[B_{0x} + B_A \tan h\left(\frac{(t-t_0)v}{L}\right) \right] \right. \\ &\quad \left. \sin\alpha + B_{0y}\cos\alpha \right\} \sin\beta + B_{0z}\cos\beta. \end{aligned} \tag{2}$$

By fitting the observed magnetic field values to Equation (2), one can ascertain the unknown parameters [t_0, L, α, β, B_A]. v refers to the solar wind bulk speed, and t_0 is the time of field polarity inversion corresponding to the current sheet center.

B_{0x}, B_{0y}, and B_{0z} are calculated by using Equation (3) with average values of the RTN components and utilizing the Euler rotations by α and β:

$$\begin{aligned} B_{0x} &= \langle B_R^{\mathrm{RTN}} \rangle \cos\alpha + \langle B_T^{\mathrm{RTN}} \rangle \sin\alpha\cos\beta \\ &\quad + \langle B_N^{\mathrm{RTN}} \rangle \sin\alpha\sin\beta, \\ B_{0y} &= -\langle B_R^{\mathrm{RTN}} \rangle \sin\alpha + \langle B_T^{\mathrm{RTN}} \rangle \cos\alpha\cos\beta \\ &\quad + \langle B_N^{\mathrm{RTN}} \rangle \cos\alpha\sin\beta, \\ B_{0z} &= -\langle B_T^{\mathrm{RTN}} \rangle \sin\beta + \langle B_N^{\mathrm{RTN}} \rangle \cos\beta. \end{aligned} \tag{3}$$

To determine the five unknown parameters, we performed a fitting process using the Levenberg–Marquardt algorithm to minimize $\chi^2 = \sum_{i=1}^{N}\left(\frac{O_i - M_i}{\sigma_i}\right)^2$ through optimization with σ_i given by the standard deviation values of each magnetic field component over the entire period considered for the analysis in this paper. To facilitate an efficient optimization procedure, we followed specific steps. Initially, we selected a set of rudimentary estimates for the five unknown parameters. Subsequently, we applied the Newton method to obtain a set of optimized initial values from the initial approximations. Finally, this set of values was fed into the Levenberg–Marquardt algorithm to refine the parameter estimation. The optimization was implemented using the MPFIT library of the IDL software (C. B. Markwardt 2009). The error associated with each fit parameter was estimated by computing the covariance matrix used in the Levenberg–Marquardt algorithm.

Figure 6 exemplifies the result of application of the HYTARO fitting method to the HCS crossing event on 2013 December 23. As can be seen, the HYTARO fitting effectively reproduces the measured magnetic field. The crossing time, t_0, is determined to be 21:47:32 on 2013 December 23. The thickness of the HCS (2L) is 14,152,000 km. Using α and β, the normal vector is determined to be [0.998, −0.053, −0.030] which specifies the orientation of the HCS plane in the RTN coordinate system. The goodness-of-fit parameter R^2 (J. H. Kim et al. 2015) is also determined.

As an alternative approach to determine the HCS thickness and orientation, we conducted minimum variance analysis (MVA, B. U. Ö. Sonnerup & L. J. Cahill 1967). The eigenvector associated with the smallest eigenvalue obtained from the MVA analysis results serves as the normal vector of the corresponding HCS plane. The magnetic field direction is expected to rotate around the normal vector in the plane of the intermediate and maximum eigenvectors (B_{int}-$B_{\max}$ plane). Figure 7 illustrates a magnetic field hodogram derived from the MVA analysis applied to the same HCS event interval as in Figure 6, exhibiting such a distinct rotation signature. The HCS thickness in the MVA analysis was calculated by projecting the solar wind velocity onto the normal vector direction and considering the velocity of Voyager 2.

To assess the error in the MVA results, a bootstrap method was employed with 1000 sample sets selected during the process. The range of the error was determined using the 1σ value of the 1000 ensemble parameter distribution.

3.2. Analysis Results for HCS Thickness and Orientation

In this section, we present the results of the HCS thickness and the orientation of HCS planes in terms of latitude and longitude of the HCS plane normal vectors. These were determined by applying the two methods described in Section 3.1 to each of the two groups of HCS events. First, the results for the 24 HCSs of the B_{T}-based group are

Table 2
Analysis Results with HYTARO Algorithm for the 24 HCS Events of the B_T-Based Group

Event ID	Current Sheet Crossing Time (t0)	Thickness [10^3 km]	Normal Vector Latitude [Degree]	Normal Vector Longitude [Degree]	Goodness of Fit (R^2)
1	2008-03-15 21:59:31	3453	−26.5	−6.4	0.587
2	2008-03-25 19:00:28	20,198	−34.3	−3.3	0.683
3	2008-10-04 01:20:34	7620	−53.6	−16.9	0.658
4	2011-10-26 23:17:18	20,986	−17.1	−17.9	0.519
5	2011-11-06 07:33:51	8682	−28.6	−10.8	0.594
6	2013-11-16 15:02:00	10,125	−32.2	−5.8	0.413
7	2013-11-27 14:11:30	43,478	−28.4	9.3	0.548
8	2013-12-23 21:47:32	14,152	−32.7	−3.0	0.568
9	2014-01-14 06:15:17	17,153	−36.4	−8.7	0.449
10	2014-04-20 08:41:58	20,896	−31.7	−5.2	0.366
11	2014-11-22 03:21:47	2176	−37.7	−15.4	0.801
12	2015-03-12 13:23:21	16,287	−36.5	−22.1	0.665
13	2015-06-10 21:30:00	32,697	−37.9	−5.9	0.262
14	2016-01-16 12:59:31	8355	−20.8	−17.9	0.632
15	2016-02-21 17:59:31	66,113	−33.6	5.6	0.319
16	2016-04-10 13:02:04	27,830	−31.3	−4.3	0.403
17	2016-07-28 16:29:31	3684	−27.6	27.4	0.635
18	2016-08-13 05:06:22	11,020	−22.9	−3.7	0.646
19	2016-10-20 14:45:35	20,758	−31.0	−13.4	0.305
20	2016-10-30 00:41:31	32,351	−28.1	−14.7	0.376
21	2017-06-05 14:01:32	2997	−35.7	−16.8	0.842
22	2017-06-19 10:53:09	4790	−31.0	−31.4	0.568
23	2018-01-11 10:58:10	15,294	−33.6	−29.9	0.624
24	2018-02-22 02:33:04	12,388	−31.1	10.0	0.503

summarized in Table 2 obtained from the HYTARO analysis and Table 3 obtained from the MVA analysis.

The HCS thickness and orientations presented in Tables 2 and 3 are summarized in Figure 8. In panels (a) and (d), the HYTARO analysis results (red) indicate that the range of thickness for the 24 HCS crossings spans from $\sim 2 \times 10^6$ to $\sim 6.6 \times 10^7$ km ($\sim$0.01 au to $\sim$0.44 au) with an average of $\sim 1.7 \times 10^7$ km ($\sim$0.1 au), and the MVA analysis (black) reveals a thickness range from $\sim 1.1 \times 10^6$ to $\sim 3 \times 10^7$ km ($\sim$0.007 au to $\sim$0.2 au) with an average of $\sim 1.4 \times 10^7$ km ($\sim$0.09 au). Therefore, the thickness values estimated from both methods fall within a qualitatively consistent range, despite some variability in the width of the ranges.

Figures 8(b) and (e) demonstrate that the latitude of the HCS normal vector, as obtained from the HYTRAO method, spans a range from $\sim -20°$ to $\sim -60°$, while those obtained from the MVA analysis distribute over an even wider range. Despite some discrepancy between the two methods, both results imply a frequent occurrence of HCSs with a significant tilt relative to the solar equator to varying degrees.

Figures 8(c) and (f) reveal that the longitude of the normal vector, as obtained from the HYTRAO method, predominantly lies around 0°. Despite some spread, a similar trend is discernible from the MVA analysis result to a reasonable degree. This implies that the HCSs are predominantly aligned to the Parker spiral field, which lies primarily in the tangential direction within the HS.

The results for the 10 HCSs of the B_N-based group are summarized in Table 4 obtained from the HYTARO analysis and in Table 5 obtained from the MVA analysis. Figure 9 shows the summary of the determined thickness and orientations of the 10 HCS events. The results in Figure 9 reveal that the inferred thickness from both fitting methods is relatively smaller by a few to several tens of percentages compared to those for the 24 HCS events of the B_T-based group in Figure 8. Specifically, for the 10 HCS crossings, the HYTARO fitting method indicates a thickness range from $\sim 5.2 \times 10^5$ to $\sim 1.3 \times 10^7$ km ($\sim$0.003 au to $\sim$0.085 au) with an average of $\sim 4 \times 10^6$ km ($\sim$0.03 au) and the MVA technique suggests a thickness range from $\sim 7.2 \times 10^5$ to $\sim 2 \times 10^7$ km ($\sim$0.005 au to $\sim$0.13 au) with an average of $\sim 6.8 \times 10^6$ km ($\sim$0.045 au). The overall distributions of the latitude and longitude of the normal vector exhibit similarities to those for the 24 HCS events identified using the tangential component.

The finding that the current sheets for the 10 HCS events of the B_N-based group are relatively thinner by up to several tens of percentages compared to those for the 24 HCS events of the B_T-based group is noteworthy. We hypothesize that the currents driving B_T polarity changes in the B_T-based group and B_N polarity changes in the B_N-based group are primarily oriented in the normal direction (so, $J \approx J_N$) and in the tangential direction (so, $J \approx J_T$), respectively. Then, if we adopt the Harris sheet model field for the current sheets, the current density is proportional to $(B_A/L)\,\mathrm{sec}\,h^2\left(\frac{y-y_0}{L}\right)$. We find that the average asymptotic value B_A for the 10 HCSs of the B_N-based group is $\sim$87% of that for the 24 HCSs of the B_T-based group, and L is smaller by up to several tens of percentages for the 10 HCSs of the B_N-based group. Consequently, the combination of these two parameters implies a narrower current profile (characterized by the smaller L) with a peak value at the center (given by (B_A/L)) that is larger by tens of percentages for the B_N-based group than for the B_T-based group. In other words, the current density profile is more sharply peaked at the center and declines more rapidly away from the center for the B_N-based group. What determines this difference between the two groups is unclear to us.

Table 3
Analysis Results with MVA Technique for the 24 HCS Events of the B_T-based Group.

Event ID	MVA Start Time[a]	MVA End Time[a]	Thickness [10^3km]	Normal Vector Latitude [Degree]	Normal Vector Longitude [Degree]	Eigenvalue Ratio ($\lambda_{int}/\lambda_{min}$)
1	2008-03-15 13:00:00	2008-03-16 08:00:00	7742	−23.3	−7.1	24.2
2	2008-03-25 01:00:00	2008-03-27 15:00:00	23,492	−19.7	−19.0	13.5
3	2008-10-02 23:00:00	2008-10-05 04:00:00	26,965	−69.3	1.9	5.1
4	2011-10-22 19:00:00	2011-10-29 01:00:00	22,885	23.6	28.7	2.4
5	2011-11-05 20:00:00	2011-11-07 02:00:00	8239	−3.5	2.3	35.8
6	2013-11-15 20:00:00	2013-11-18 00:00:00	4697	18.0	−37.3	7.1
7	2013-11-25 19:00:00	2013-11-29 23:00:00	43,828	−68.4	5.1	1.3
8	2013-12-23 09:00:00	2013-12-24 19:00:00	17,775	−84.4	47.7	16.2
9	2014-01-12 12:00:00	2014-01-15 18:00:00	33,499	−71.9	−19.7	7.7
10	2014-04-19 04:00:00	2014-04-21 11:00:00	13,204	−22.2	−18.2	9.2
11	2014-11-21 16:00:00	2014-11-22 23:00:00	7447	−34.6	−13.6	5.6
12	2015-03-10 08:00:00	2015-03-14 04:00:00	706	−13.8	−44.0	15.0
13	2015-06-08 20:00:00	2015-06-13 06:00:00	26,387	−27.9	−18.9	2.4
14	2016-01-15 08:00:00	2016-01-17 18:00:00	11,137	−0.6	−6.6	7.4
15	2016-02-18 08:00:00	2016-02-25 16:00:00	58,846	−1.3	34.8	5.2
16	2016-04-08 20:00:00	2016-04-12 14:00:00	22,090	−2.6	−1.2	4.0
17	2016-07-28 02:00:00	2016-07-29 02:00:00	7965	−2.1	18.0	29.2
18	2016-08-11 20:00:00	2016-08-16 00:00:00	33,076	−22.6	−2.2	6.6
19	2016-10-18 13:00:00	2016-10-22 15:00:00	5518	0.1	−28.2	15.1
20	2016-10-26 20:00:00	2016-11-02 00:00:00	36,930	−8.4	−5.2	9.3
21	2017-06-05 03:00:00	2017-06-06 00:00:00	697	15.0	−33.1	13.0
22	2017-06-18 09:00:00	2017-06-20 15:00:00	4373	3.7	−50.0	9.3
23	2018-01-08 14:00:00	2018-01-13 18:00:00	5725	−24.7	−40.3	5.3
24	2018-02-21 00:00:00	2018-02-23 02:00:00	21,957	−51.7	8.2	5.0

Note.
[a] The start and end times of the interval to which the MVA technique was applied.

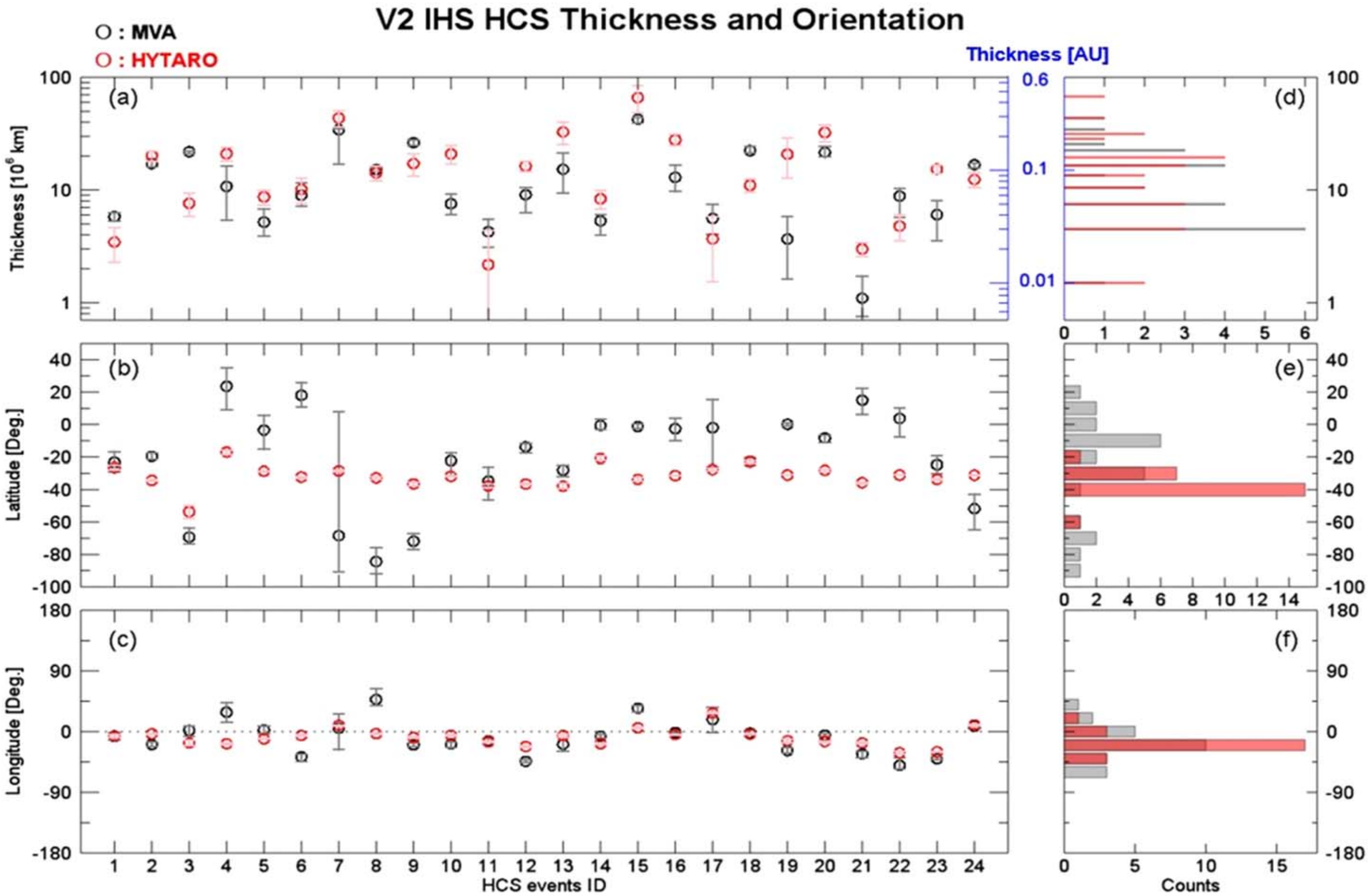

Figure 8. Structural analysis results of 24 HCSs of the B_T-based group identified by Voyager 2 B_T component. (a) HCS thickness (b) latitude of the normal vector, and (c) longitude of the normal vector, as defined in Figure 5. (d)–(f) Histograms of each result. In all panels the results of HYTARO are indicated by the red color, while the results of MVA are represented by black or gray.

Table 4
Analysis Results with HYTARO Algorithm for the 10 HCS Events of the B_N-based Group

Event ID	Current Sheet Crossing Time (t0)	Thickness [10^3 km]	Normal Vector Latitude [Degree]	Normal Vector Longitude [Degree]	Goodness of Fit (R^2)
1	2012-06-26 09:49:17	4097	−31.0	0.0	0.528
2	2012-07-05 20:45:58	12,716	−17.0	−8.6	0.711
3	2013-07-17 01:04:29	518	−19.7	5.7	0.697
4	2013-07-24 03:43:06	2568	−23.5	2.9	0.601
5	2013-08-14 16:43:19	5084	−30.7	0.1	0.405
6	2014-03-10 03:43:20	774	−43.8	0.7	0.375
7	2014-03-22 02:17:24	1543	−29.1	−1.8	0.597
8	2014-08-24 20:26:01	5052	−7.6	1.5	0.529
9	2015-09-29 01:18:43	6195	−31.1	−0.1	0.398
10	2015-11-21 11:05:34	1641	−21.1	−12.6	0.765

3.3. Nature of the HCS Planes as a Discontinuity

We further examined whether the selected HCSs exhibit characteristics closer to an RD or a TD by assessing the ratio $B_{\mathrm{normal}}/|B|$ where B_{normal} refers to the normal component of the magnetic field to the HCS plane derived by projecting the magnetic field onto the normal vector obtained from the MVA results. The distribution of $B_{\mathrm{normal}}/|B|$ for the total 34 HCSs is depicted in Figure 10. The distribution is rather broad with an average value of 0.4. Nevertheless, it is reasonable to conclude that for a large fraction of the events, the ratio $B_{\mathrm{normal}}/|B|$ is nonnegligible or even substantial, implying the possibility of an RD.

4. Discussion

It is insightful to compare the thickness values of the HCSs estimated in Section 3.2 with significant characteristic scale lengths. First, we find that the HCS thickness values (on the order of 10^5–10^7 km depending on methods of event selection and fitting techniques) are much larger than the proton inertial length, which ranges from ∼4000 km to ∼6000 km for the

Table 5
Analysis Results with MVA Technique for the 10 HCS Events of the B_N-based Group

Event ID	MVA Start Time	MVA End Time	Thickness [10^3 km]	Normal Vector Latitude [Degree]	Normal Vector Longitude [Degree]	Eigenvalue Ratio ($\lambda_{int}/\lambda_{min}$)
1	2012-06-25 23:00:00	2012-06-27 08:00:00	1500	−41.9	−58.4	31.0
2	2012-07-04 02:00:00	2012-07-06 22:00:00	19,934	−4.9	36.3	5.1
3	2013-07-16 16:00:00	2013-07-17 07:00:00	4546	−25.7	2.9	6.4
4	2013-07-24 01:00:00	2013-07-24 06:00:00	723	−10.2	−4.0	41.7
5	2013-08-14 16:00:00	2013-08-15 05:00:00	1584	−36.6	−28.0	11.7
6	2014-03-09 17:00:00	2014-03-10 17:00:00	8887	−26.1	11.8	10.9
7	2014-03-21 22:00:00	2014-03-22 09:00:00	2552	−38.8	2.4	3.9
8	2014-08-23 21:00:00	2014-08-26 02:00:00	14,991	−17.8	42.5	11.6
9	2015-09-28 17:00:00	2015-09-29 18:00:00	5811	−16.2	−8.6	177.0
10	2015-11-20 14:00:00	2015-11-21 23:00:00	7431	−20.7	−7.8	3.0

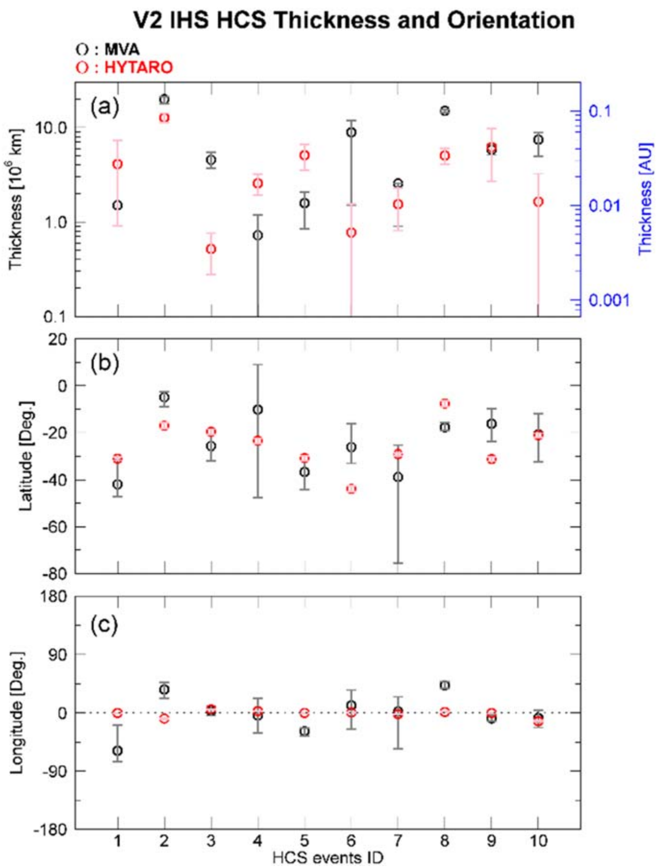

Figure 9. Structure analysis results of 10 HCSs of the B_N-based group identified by utilizing the polarity change in the normal component of the magnetic field. (a) HCS thickness, (b) HCS normal vector latitude, and (c) HCS normal vector longitude. In (a), the lower limit of the error bar for the HYTRAO result for Event 6 extends to $\sim 0.007 \times 10^6$ km.

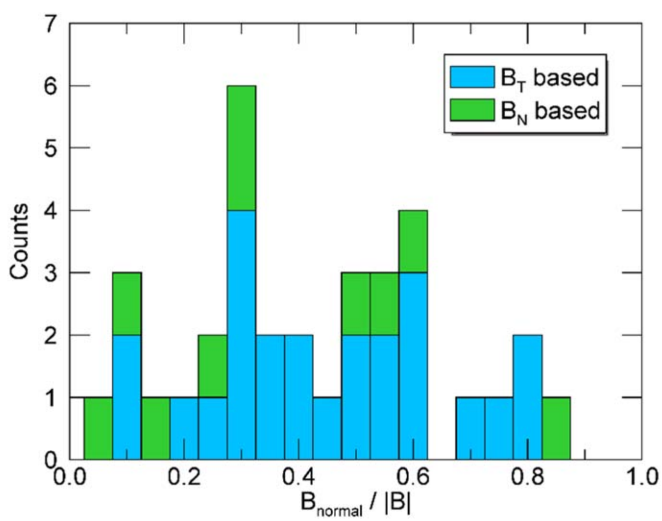

Figure 10. Statistics of the ratio $B_{normal}/|B|$, where B_{normal} refers to the normal vector to HCS planes. Blue columns represents the statistics for the 24 HCSs of the B_T-based group, and green columns represents those for the 10 HCSs of the B_N-based group.

identified HCS event intervals. This may imply that the physical conditions conducive to the HCS events in the HS identified in this work are unfavorable for magnetic reconnection (P. A. Cassak et al. 2005; M. Yamada 2007).

Furthermore, we find that the average thickness of the HCSs is comparable to the gyro radius of protons with $\sim$1 MeV (or equivalently $\sim$10 gyro radii of pickup protons with 10 keV) in the HS, implying a potential impact on the dynamics of energetic particles including anomalous cosmic rays within the HS.

Additionally, it is valuable to assess the thickness of our HCSs in the HS in comparison with previous works within a similar context. To facilitate this comparison, we have compiled a summary of HCS thickness available from relevant literature in Table 6. These previous works determined HCSs at various heliospheric distances, ranging from close proximity to the Sun as observed by the PSP to several au by Pioneer 11, but no previous report on the HCS thickness based on a comprehensive analysis is available within the HS. The summary in Table 6 indicates that the thickness of HCSs within the HS estimated in the present work (ranging from $\sim 10^5$ to $\sim 10^7$ km) mostly surpasses those observed at other distances closer to the Sun in previous works (typically on the order of 10^3–10^6 km).

It remains unclear to us what controls the thickness of HCSs in the HS, while we acknowledge the proposition that the HCS thickness near the Earth is related to the magnetic pressure gradient of the solar magnetic field (C.-C. Wu et al. 2016). On the other hand, we recognize the proposal made by J. F. Drake et al. (2010) and M. Opher et al. (2011) regarding the sectored magnetic field behavior at the HP. According to their suggestion, the HCSs accumulate as it nears the HP, causing a narrowing of the current sheets that divide the sectors and potentially initiating collisionless magnetic reconnection. This particular aspect has not been explored within the scope of our study.

We emphasize that the primary goal of the present work has been to focus on large-scale HCSs that could be unequivocally identified as sector boundaries rather than local current sheets by imposing a strict set of selection criteria as described in Section 2. However, due to limitations in the hourly resolution data used in this work, we cannot rule out the potential oversight of thinner current sheets and multiple current sheets (M. I. Pudovkin et al. 1999; E. J. Smith 2001; J. T. Gosling et al. 2006a, 2006b; C. Foullon et al. 2009) that were not captured in Section 3. Such thinner or multiple current sheets may be examined with higher time resolution data (48 s), which we plan to pursue in a future project.

The rather broad distribution of latitude of the HCS normal vector, as discussed in Section 3.2, is similar to observations near 1 au (S. Shodhan et al. 1994; R. P. Lepping et al. 1996; J. J. Blanco et al. 2008; K. Liou & C.-C. Wu 2021; D. Arrazola et al. 2022). This clearly implies frequent occurrence of a tilted HCS within the HS.

Several studies documented the existence of the merged interaction region (MIR) within the HS (J. D. Richardson et al. 2017; L. F. Burlaga et al. 2018, 2021). In our investigation, we scrutinized the time intervals of HCS crossings concerning the reported MIRs. Notably, we found that some of our HCS events occurred during the MIRs. However, we found no significant difference in any aspect between these HCS events and the remaining HCS events in our analysis.

In future research, it would be valuable to explore the evolution of HCS thickness with increasing distance from the Sun using Voyager observations. Additionally, investigating the occurrence rate of high-tilt HCS during solar minimum and

Table 6
Summary of HCS Thickness Reported in Previous Papers

Authors	Spacecraft Location	Year	Thickness [km]	Analysis Method	Number of Events	Time Resolution
B. Bavassano et al. (1976)	Pioneer 8 at 1 au	1968	1×10^3–2×10^4	MVA	4	1.3–1.7 s
E. J. Smith et al. (1978)	Pioneer 11 at 3.7–5 au	1974-1976	1×10^4–1×10^6	…	…	…
L. Klein & Burlaga (1980)	IMP 6 at 1 au	1971-1974	1×10^4–1×10^6	MVA	18	0.08 s
K. W. Behannon et al. (1981)	Helios 1 at 0.31–1 au	1974-1975	4×10^4–1×10^5	MVA	105	8 s
U. Villante & R. Bruno (1982)	Helios 2 at 0.33–0.96 au	1976	1×10^4–6×10^4	MVA	14	6 s
D. Winterhalter et al. (1994)	ISEE 3 at 1 au	1978-1979	3×10^3–1×10^4	MVA	19	0.17 s
R. P. Lepping et al. (1996)	Wind at 1 au	1995	6×10^4	MVA	212	3 s–1 minute
J. J. Blanco et al. (2008)	Wind at 1 au	1995-2001	$9 \pm 5 \times 10^5$	HYTARO	165	…
T. D. Phan et al. (2020)	PSP at 35.7–75.2 $R_\odot$	2018	3.1×10^3–2.9×10^5	MVA	6	< 0.2 s
T. D. Phan et al. (2021)	PSP at 29.5–107 $R_\odot$	2018-2020	1.7×10^3–1.6×10^5	MVA	6	< 0.2 s
K. Liou & C.-C. Wu (2021)	Wind at 1 au	1995-2020	$1.1 \pm 0.04 \times 10^5$	HYTARO	1197	3 s
D. Arrazola et al. (2022)	Wind at 1 au	1995-1997	6×10^3–1.2×10^6	HYTARO	40	…

solar maximum could be insightful. These analyzes may provide a deeper understanding of the dynamic behavior of the HCS and its interaction with the solar cycle.

5. Summary and Conclusion

In this study, we analyzed HCS crossing events within the HS using data obtained from Voyager 2 observations. The analysis utilized Voyager magnetic field and plasma data, primarily based on 1 hr resolution data. To ensure robust HCS event selection, stringent criteria were applied, considering gaps and uncertainties in data. Consequently, we first identified 24 HCSs based on the polarity changes in the tangential magnetic field component that were clearly associated with sector boundaries over an 11 yr period spanning from 2008 to 2018. To be complete, we additionally identified 10 HCSs based on the polarity changes in the normal magnetic field component. Overall, more HCS events were identified during solar maximum when the HCS expanded to higher latitudes while Voyager 2's position was situated at a latitude of $-31°$ relative to the solar equatorial plane. Across HCS crossings, a discernible but weak trend was observed, accompanied by significant standard deviations in key parameters, including a decrease in magnetic field intensity, a slight decrease in solar wind speed, as well as an increase in proton density. Despite their weakness, these trends qualitatively align with findings from previous studies on HCSs near 1 au.

The primary focus of this study is to determine the thickness and orientation of the identified HCSs by applying two different methods, i.e., the HYTARO algorithm and MVA. The determined thickness of the HCSs is mostly large, averaging around $\sim$0.03 to $\sim$0.1 au, depending on methods of event selection and fitting techniques. This substantial value, considerably larger than the proton inertial length of the corresponding events, indicates conditions not favorable for magnetic reconnection. We found a notably broad distribution of the latitude of the HCS normal vector, similar to that observed near 1 au. The longitudinal orientation of the normal vector was found to be perpendicular to the Parker spiral field, consistent with previous findings at other heliospheric distances (B. T. Thomas & E. J. Smith 1981; M. E. Burton et al. 1994; R. P. Lepping et al. 1996; J. J. Blanco et al. 2008; K. Liou & C.-C. Wu 2021). Finally, we assessed the extent to which the HCS planes align closer to either an RD or a TD and concluded that for a large fraction of the events, the ratio $B_{\mathrm{normal}}/|B|$ is nonnegligible or even substantial, implying the possibility of an RD. Readers should be cautioned that all these results are valid within the limits of the 1 hr resolution data and may be subject to potential errors due to data uncertainties.

Acknowledgments

This work was supported under the framework of international cooperation program managed by the National Research Foundation of Korea (2023K2A9A2A22091089, FY2023). This work was also supported by the National Research Foundation of Korea (NRF) grant funded by the Korea government (MSIT), NRF-2020R1A2C1013159, and by the National Research Foundation of Korea (NRF) grant funded by the Korea government (MSIT) (RS-2024-00454886). The authors acknowledge the NASA National Space Data Center and the Space Physics Data Facility and Robert Candey for usage of Voyager 2 data from https://cdaweb.gsfc.nasa.gov. D.C. acknowledges D. Arrazola for his help with the HYTRAO fitting technique during the course of this work.

ORCID iDs

Dae-Young Lee https://orcid.org/0000-0001-9994-7277
Kyung-Eun Choi https://orcid.org/0000-0003-2054-6011

References

Alfvén, H. 1977, RvGSP, 15, 271
Arrazola, D., Blanco, J. J., & Hidalgo, M. A. 2022, A&A, 660, A12
Bavassano, B., Dobrowolny, M., & Mariani, F. 1976, JGR, 81, 1
Behannon, K. W., Acuna, M. H., Burlaga, L. F., et al. 1977, SSRv, 21, 235
Behannon, K. W., Neubauer, F. M., & Barnstorf, H. 1981, JGR, 86, 3273
Blanco, J. J., Rodriguez-Pacheco, J., Hidalgo, M. A., & Sequeiros, J. 2008, JASTP, 70, 226
Blanco, J. J., Rodriguez-Pacheco, J., & Sequeiros, J. 2003, SoPh, 213, 147
Borrini, G., Gosling, J. T., Bame, S. J., Feldman, W. C., & Wilcox, J. M. 1981, JGR, 86, 4565
Bridge, H. S., Belcher, R. J., Butler, R. J., et al. 1977, SSRv, 21, 259
Burlaga, L. F., Berdichevsky, D. B., Jian, L. K., et al. 2021, ApJ, 906, 119
Burlaga, L. F., Ness, N. F., Acuna, M. H., et al. 2008, Natur, 454, 75
Burlaga, L. F., Ness, N. F., Florinski, V., & Heerikhuisen, J. 2014, ApJ, 792, 134
Burlaga, L. F., Ness, N. F., Wang, Y.-M., & Sheely, N. R. 2002, JGRA, 107, 1410
Burlaga, L. F., Ness, N. F., Richardson, J. D., Decker, R. B., & Krimigis, S. M. 2016, ApJ, 818, 147
Burlaga, L. F., Ness, N. F., & Richardson, J. D. 2017, ApJ, 841, 47
Burlaga, L. F., Ness, N. F., & Richardson, J. D. 2018, ApJ, 861, 9
Burton, M. E., Crooker, N. U., Siscoe, G. L., & Smith, E. J. 1994, JGR, 99, 1
Cassak, P. A., Shay, M. A., & Drake, J. F. 2005, PhRvL, 95, 235002
Crooker, N. U., Huang, C.-L., Lamassa, S. M., et al. 2004, JGRA, 109, A03107
Drake, J. F., Opher, M., Swisdak, M., & Chamoun, J. N. 2010, ApJ, 709, 963

Foullon, C., Lavraud, B., Wardle, N. C., et al. 2009, SoPh, 259, 389
Gosling, J. T., Borrini, G., Asbridge, J. R., et al. 1981, JGR, 86, 5438
Gosling, J. T., Eriksson, S., & Schwenn, R. 2006a, JGRA, 111, A10102
Gosling, J. T., McComas, D. J., Skoug, R. M., & Smith, C. W. 2006b, GeoRL, 33, L17102
Harris, E. G. 1962, NCim, 23, 115
Hoeksema, J. T. 1991, AdSpR, 11, 15
Hoeksema, J. T. 1995, SSRv, 72, 137
Jokipii, J. R., & Thomas, B. 1981, ApJ, 243, 1115
Khabarova, O., Zank, G. P., Li, G., et al. 2015, ApJ, 808, 181
Kim, J. H., Lee, D. Y., Cho, J. H., et al. 2015, JGRA, 120, 2819
Klein, L., & Burlaga, L. F. 1980, JGR, 85, 2269
Lavraud, B., Fargette, N., Reville, V., et al. 2020, ApJL, 894, L19
Lepping, R. P., Szabo, A., Peredo, M., & Hoeksema, J. T. 1996, GeoRL, 23, 1199
Liou, K., & Wu, C.-C. 2021, ApJ, 920, 39
Liu, Y. C.-M., Huang, J., Wang, C., et al. 2014, JGRA, 119, 8721
Markwardt, C., B. 2009, in Proc. ADASS XVIII, ASP Conf. Ser., Vol. 411, ed. D. Bohlender, P. Dowler, & D. Durand (San Francisco, CA: ASP), 251
Opher, M., Drake, J. F., Swisdak, M., et al. 2011, ApJ, 734, 71
Owens, M. J., Crooker, N. U., & Lockwood, M. 2013, JGRA, 118, 1868
Phan, T. D., Bale, S. D., Eastwood, J. P., et al. 2020, ApJS, 246, 34
Phan, T. D., Lavraud, B., Halekas, J. S., et al. 2021, A&A, 650, A13
Pudovkin, M. I., Runov, A. V., Zaitseva, S. A., Besser, B. P., & Meiser, C.-V. 1999, SoPh, 184, 173
Richardson, J. D., Wang, C., Liu, Y. D., et al. 2017, ApJ, 834, 190
Shodhan, S., Crooker, N. U., Hughes, W. J., & Siscoe, G. L. 1994, JGR, 99, 2531
Simunac, K. D. C., Galvin, A. B., Farrugia, C. J., et al. 2012, SoPh, 281, 423
Smith, E. J. 2001, JGR, 106, 15819
Smith, E. J., Tsurutani, B. T., & Rosenberg, R. L. 1978, JGR, 83, 717
Sonnerup, B. U. Ö., & Cahill, L. J. 1967, JGR, 72, 171
Stone, E. C., Cummings, A. C., Heikkila, B. C., & Lal, N. 2019, NatAs, 3, 1013
Stone, E. C., Cummings, A. C., McDonald, F. B., et al. 2008, Natur, 454, 71
Suess, S. T., Ko, Y. K., von Steiger, R., & Moore, R. L. 2009, JGRA, 114, A04103
Szabo, A., Larson, D., Whittlesey, P., et al. 2020, ApJS, 246, 47
Thomas, B. T., & Smith, E. J. 1981, JGR, 86, 11105
Villante, U., & Bruno, R. 1982, JGR, 87, 607
Wilcox, J. M., & Ness, N. F. 1965, JGR, 70, 5793
Winterhalter, D., Smith, E. J., Burton, M. E., Murphy, N., & McComas, D. J. 1994, JGR, 99, 6667
Wu, C.-C., Liou, K., Wu, S. T., & Dryer, M. 2016, in AIP Conference Proc. 1720, Solar Wind 14 (Melville, NY: AIP), 040021
Yamada, M. 2007, PhPl, 14, 058102
Zharkova, V. V., & Khabarova, O. V. 2012, ApJ, 752, 35